Supplementary Information

Near-unity spontaneous emission factor InP surface-emitting lasers based on quasi-bound states in the continuum

Wei Wen Wong[1*], Xiaoying Huang[1], Olivier Lee Cheong Lem[2], Chennupati Jagadish[1], and Hark Hoe Tan[1*]

[1]Australian Research Council Centre of Excellence for Transformative Meta-Optical Systems, Department of Electronic Materials Engineering, Research School of Physics, The Australian National University, Canberra, ACT 2600, Australia.

[2]Australian National Fabrication Facility, Research School of Physics, The Australian National University, Canberra, ACT 2600, Australia.

Email addresses:
***weiwen.wong@anu.edu.au**
xiaoying.huang@anu.edu.au
laurent.leecheonglem@anu.edu.au
chennupati.jagadish@anu.edu.au
***hoe.tan@anu.edu.au**

[*]Corresponding authors:

Dr. Wei Wen Wong
Australian Research Council Centre of Excellence for Transformative Meta-Optical Systems,
Department of Electronic Materials Engineering Research School of Physics, The Australian National University, Canberra, ACT 2600 Australia
Email: weiwen.wong@anu.edu.au
Phone: +61 4 1395 1829

Prof. Hark Hoe Tan
Australian Research Council Centre of Excellence for Transformative Meta-Optical Systems,
Department of Electronic Materials Engineering Research School of Physics, The Australian National University, Canberra, ACT 2600 Australia
Email: hoe.tan@anu.edu.au
Phone: +61 2 6125 0356

Keywords:

Bound states in the continuum, photonic crystal surface-emitting lasers, III-V semiconductor nanosheets, selective area epitaxy, InP

Contents

Section A: Further details on device fabrication

Fig. S1 summarises the etching-free, bottom-up approach used for laser fabrication in this work. The fabrication process starts with the deposition and patterning of a SiO_2 growth mask on an InP (111)A substrate. The key to growing the nanosheet structures is to strategically align the slot openings in the SAE growth mask along the $[1\bar{1}0]$ direction on an InP (111)A substrate. As demonstrated in our previous work[1], aligning the mask openings along this specific crystallographic direction facilitates the elongation of a pair of WZ-phase $\{1\bar{1}00\}$ sidewall facets via the mask confinement effect during SAE, yielding a hexagonal nanosheet morphology with large height-to-width aspect ratio. Other than eliminating the need for top-down dry-etching that often results in rough sidewalls, employing this shape engineering approach for laser fabrication also makes the grown nanostructures functioning as both the active gain medium and the laser cavity at the same time, resulting in optimal spatial overlap between the lasing mode and the active region. Finally, the growth mask was removed by wet etching after nanosheet epitaxy to create the air cladding layer at the nanosheet/substrate interface. Fig. S2a and S2b are low-magnification ratio scanning electron microscopy (SEM) images showing multiple laser arrays and the array with asymmetry parameter α = 0.1, respectively. The uniform morphology across the arrays demonstrates the excellent scalability of our bottom-up fabrication process.

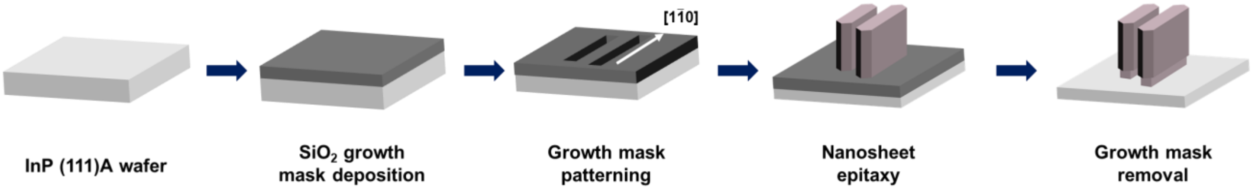

Fig. S1 Schematic diagram illustrating the etching-free laser fabrication process. High aspect ratio nanosheet structures were grown by the SAE technique on a layer of SiO_2 growth mask patterned with $[1\bar{1}0]$-oriented slot openings. The growth mask layer was removed after epitaxy to create a layer of air cladding at the bottom of the nanosheets. See Methods in the main text for further details of the epitaxy process.

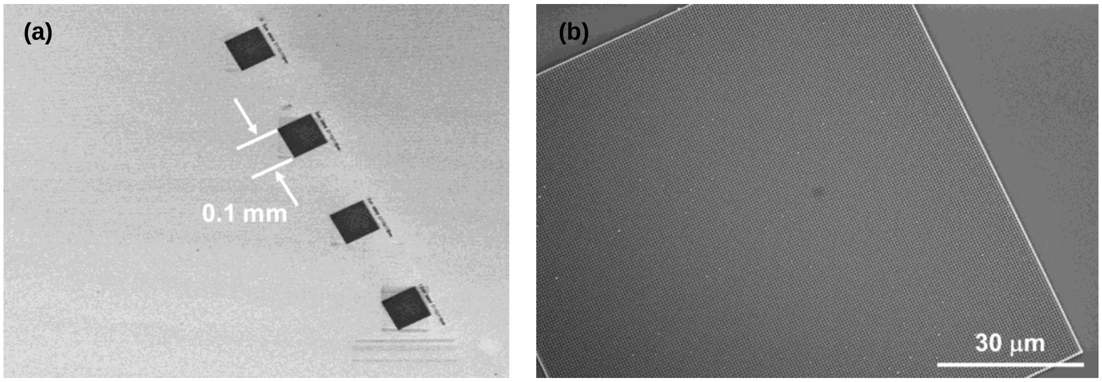

Fig. S2 Low-magnification ratio SEM images of the fabricated laser arrays. (a) SEM image showing multiple laser arrays with different α values. **(b)** SEM image showing a single laser array with α = 0.1.

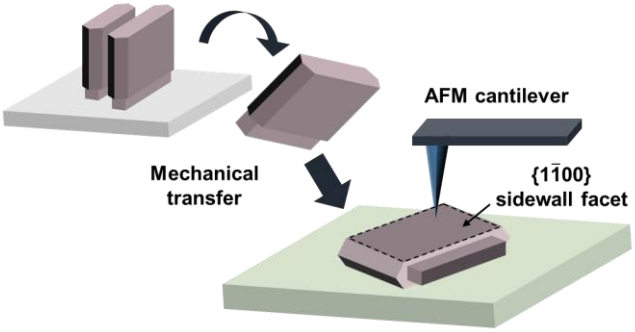

Fig. S3 Schematic diagram illustrating the process of mechanically removing and transferring as-grown nanosheets for AFM measurements. See Methods of the main text for further details on AFM sample preparation.

To perform atomic force microscopy (AFM) topography on the dominant $\{1\bar{1}00\}$ sidewall facet of a single nanosheet, we mechanically removed and transferred as-grown nanosheets on to a Si substrate, as illustrated by the schematic diagram in Fig. S3.

Section B: Bandstructure and side mode simulations

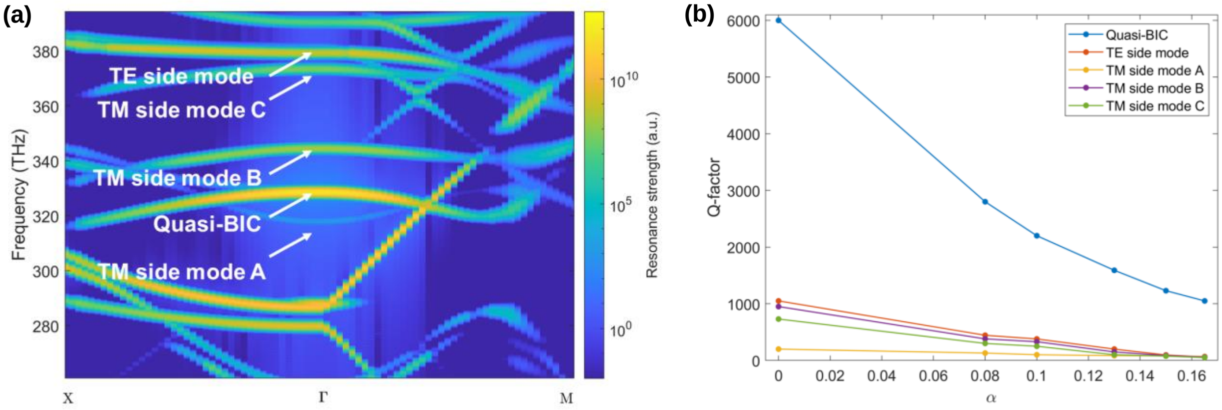

Fig. S4 Side modes lying within the material gain bandwidth of WZ-phase InP. (a) Simulated bandstructure of the device with $\alpha = 0$. The spectral positions of the quasi-BIC lasing mode and other side modes at the Γ-point are indicated by the arrows. (b) Simulated Q-factors of these modes as functions of α. The quasi-BIC mode has a finite Q-factor at $\alpha = 0$ due to non-radiative damping provided by the lossy substrate.

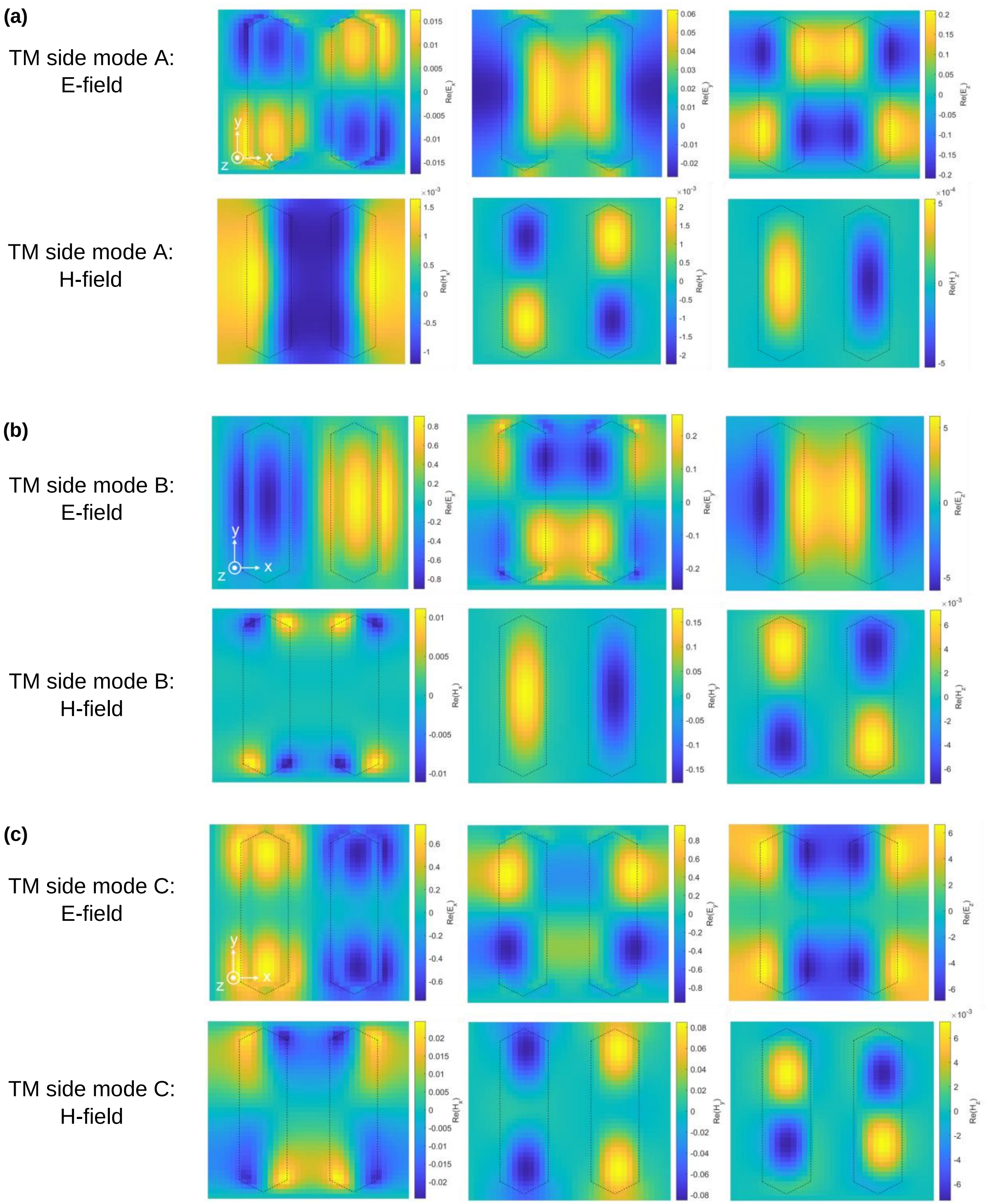

Fig. S5 Simulated field distribution profiles of the TM side modes. (a – c) Simulated field distribution profiles for TM side modes A, B, and C, respectively, which have their spectral positions in the bandstructure indicated in Fig. S4a. Top panels: real parts of the (from left to right) *x*, *y*, and *z*-components of the electric field vectors. Bottom panels: real parts of the (from left to right) *x*, *y*, and *z*-components of the magnetic field vectors.

In this section, we provide additional information regarding the transverse magnetic (TM) and transverse electric (TE) side modes that lie within the gain and spontaneous emission bandwidths of WZ-phase InP. The spectral positions of these side modes are indicated in the simulated bandstructure in Fig. S4a. The simulated Q-factors of these modes (along with that of the quasi-BIC lasing mode) are plotted in Fig. S4b as a function of α. Fig. S5a – c, on the other hand, are the simulated field distribution profiles which reveal the TM-like field polarisations in TM side modes A, B, and C, respectively. Fig. S6, on the other hand, compares the mode profiles of the competing TE side mode with that of the BIC mode. Leakage loss into the substrate is evidently more prominent in the TE side mode, which explains its much lower Q-factor and the broader fitted linewidth corresponding to this mode in the ASE spectra discussed in Fig. 4 of the main text.

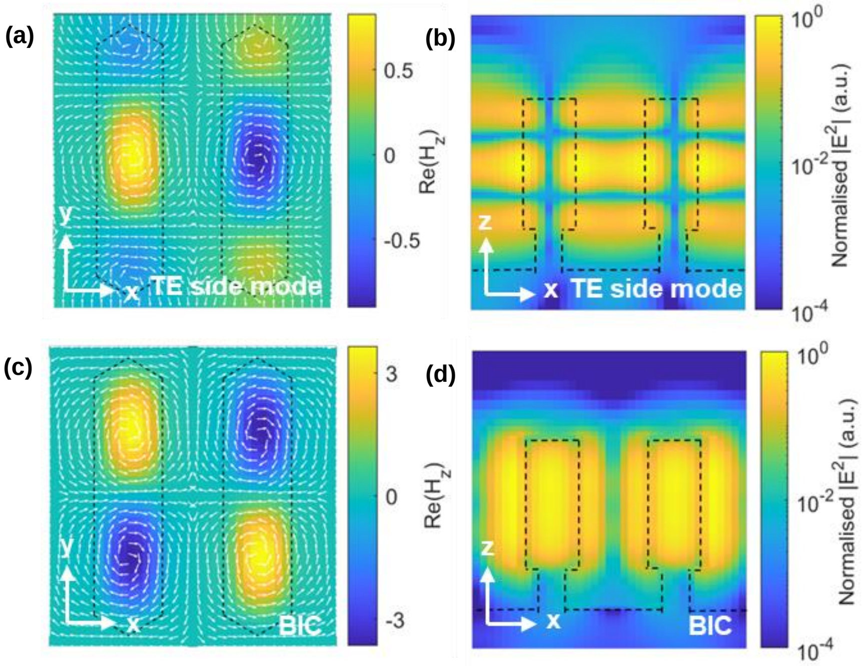

Fig. S6 Simulated field distribution profiles of the side mode (a & b) and the BIC mode with $\alpha = 0$ (c & d) at the Γ-point. The colour maps and the length of the white arrows represent the magnitudes of the out-of-plane magnetic field vector and the in-plane electric field vector, respectively. **(a)** and **(c)** are the *xy*-plane H_z profiles (overlaid with white arrows representing the in-plane electric field vectors), whereas **(b)** and **(d)** are the *xz*-plane electric field intensity profiles, plotted on logarithmic scales. The nanosheet positions are indicated by the black dotted lines.

Section C: Additional far-field simulation and characterisation data

In this section, we provide further details on far-field emission pattern simulation and back focal plane measurements. Despite the directional far-field emission, the significant beam divergence from the normal direction in the $\alpha = 0.10$ device (discussed in Fig. 3 of the main text) warrants further investigation. Since the beam divergence angle of PCSELs is inversely proportional to the effective emission aperture size[2,3], we analysed the effect of the finite excitation area in our device by numerically simulating the far-field projections from an infinite array device with varying illumination sizes (see Methods of the main text). As shown in Fig. S7a, while the simulation results reflect the expected scaling trend in the divergence angle, for a 16 × 16 array the experimental divergence angle is almost 2.5 times larger than the simulation result (see inset of Fig. S7a). We then compare the beam divergence angles simulated with the two different configurations illustrated in Fig. S7b. The first configuration simply calculates the far-field emission patterns from different emission areas in an infinite array of lossless nanosheet pairs. A Gaussian weighting function is used to modify the far-field projection from the periodic array according to the desired number of unit cell periods. On the other hand, the second configuration is designed to emulate the actual optical pumping scenario in our experiments. An island of lossless nanosheet pairs (assumed to be pumped to transparency) is surrounded by a boundary of lossy nanosheets, which represents the unpumped unit cells. The simulation results in Fig. S7a indicate that the larger in-plane leakage losses in the second scenario results in larger beam divergence angles, which correspond well to experimental observation. This also suggests that beam divergence can be potentially alleviated by reducing in-plane leakage in the finite-sized device through approaches such as hetero-lattice photonic crystal[4,5]. The limited number of data points for the second scenario is due to the impractically long simulation time required for very large finite arrays. Very small finite arrays, on the other hand, no longer support the quasi-BIC mode due to severe in-plane leakage loss.

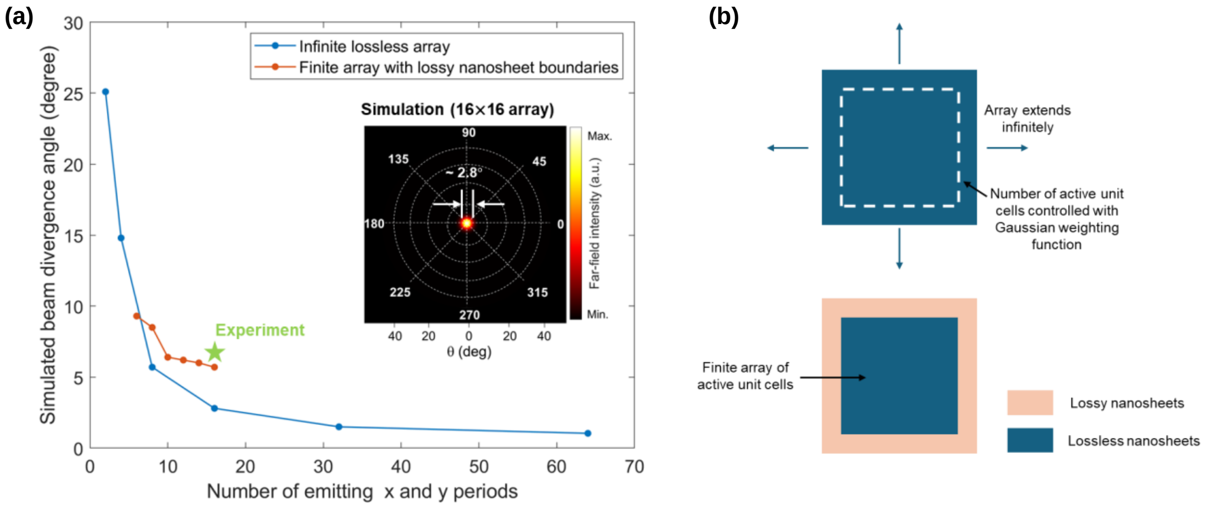

Fig. S7 Beam divergence angle simulated as a function of the active emission area. (a) Simulated beam divergence angles for two different simulation configurations. The experimentally measured beam divergence angle is overlaid on to the plot. Inset shows the far-field emission pattern for 16×16 periods of lossless unit cells, simulated with the top configuration illustrated in **(b)**. **(b)** Schematic diagrams illustrating the two different simulation configurations. The first (top) configuration modifies the far-field projection from a periodic array of lossless nanosheets with a Gaussian weighting function that reflects the number of emitting unit cells. The second (bottom) configuration directly simulates the far-field projection from a finite array of lossless (pumped) nanosheets that is surrounded by a boundary of lossy (unpumped) nanosheets, in order to mimic the actual optical pumping in experiments.

Furthermore, to unveil the polarisation of the laser beam, we simulate the *x*- and *y*-resolved vector components of the electric field of the quasi-BIC lasing mode in the far-field. The simulation results shown in Fig. S8 reveal that the amplitude of the *x* vector component of the electric field in the far-field is an order of magnitude larger than its *y*-oriented counterpart, indicating that the quasi-BIC beam is linearly polarised in the *x*-direction (orthogonal to the nanosheet long axis). In Fig. S9 we provide the back focal plane images for all the devices discussed in Fig. 4 of the main text, which were measured at pump fluences of around 20 % above their respective lasing thresholds. The significantly broader beam measured in the device with $\alpha = 0.165$ is most likely due to worsened in-plane leakage loss in the device.

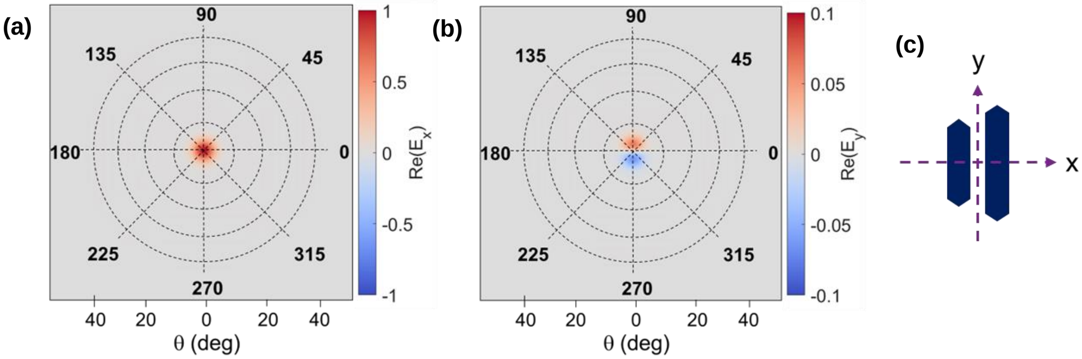

Fig. S8 Beam polarisation in the far-field. Simulated **(a)** *x* and **(b)** *y* vector components of the electric field in the far-field for the quasi-BIC mode with $\alpha = 0.10$, with 16×16 periods of active unit cells. **(c)** Schematic diagram that illustrates the *x* and *y* directions relative to the nanosheet orientation.

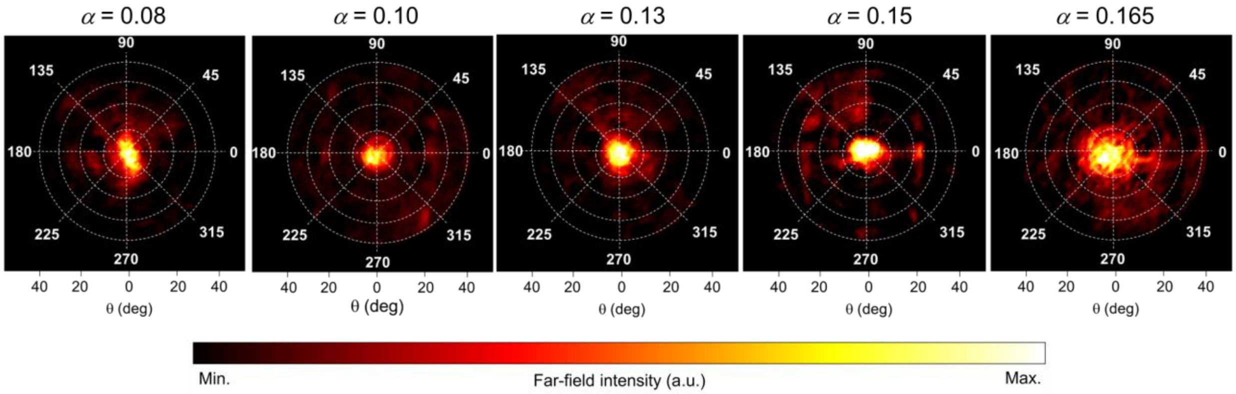

Fig. S9 Back focal plane images of the lasing devices with varying α values. Back focal plane images were measured using a 60× objective lens used for signal collection (see Methods of the main text for further details), at pump fluences of approximately 20 % above the respective lasing thresholds of the devices.

Section D: Material gain modelling

The material gain g is modelled using the following expression[6]:

$$g(\hbar\omega) = \frac{\pi e^2}{n_r c \varepsilon_0 m_0^2 \omega} |M|^2 \int \rho_r(E) \cdot [f_c(E) - f_v(E)] \cdot \ell(E - \hbar\omega)\, dE, \tag{S1}$$

where e, n_r, c, ε_0, m_0, $\hbar$, ω, and $|M|^2$ are respectively the electron charge, refractive index of InP, speed of light in vacuum, vacuum permittivity, electron mass, reduced Planck constant, radial frequency of photon, and momentum matrix element of bulk InP. $\rho_r(E)$ is the reduced density of states function, whereas $f_c(E)$ and $f_v(E)$ are the Fermi-Dirac distribution of charge carriers in CB and VB, respectively. $\ell(E - \hbar\omega)$ is a sech lineshape broadening function included to account for energy broadening of electron-hole states[7].g is a function of the Fermi-Dirac distribution functions $f_c(E)$ and $f_v(E)$, which are functions of the bandgap energy, injected carrier density, and temperature.

The bandgap energy is modelled by considering only the fundamental band-to-band transition in WZ-phase InP (transition from Γ_7^C conduction band to Γ_9^V valence band, or valence band A)[8–10]. The bandgap energy as a function of temperature is modelled with the following equation[9]:

$$E_g(T) = E_B - a\left(1 + \left(\frac{2}{e^{\theta/T} - 1}\right)\right), \tag{S2}$$

where E_B, a, and θ are experimentally-fitted parameters obtained via photoluminescence (PL) and PL excitation (PLE) measurements of WZ InP nanowires. The values of these parameters are listed in Table S1. We model the carrier density N by:

$$N = \frac{\eta_{pump} \cdot P_{avg}}{f_{pump} \cdot E_{pump} \cdot V}, \tag{S3}$$

where P_{avg}, f_{pump}, E_{pump} ($E_{pump} = \frac{hc}{\lambda_{pump}}$), and V are the average power, pulse repetition rate (10 MHz), energy of pump photons of the 520 nm (λ_{pump}) femtosecond pulsed laser used in our PL system, and the volume of the active region, respectively. η_{pump}, the pump efficiency, is calculated by the following equation[7,11]:

$$\eta = \frac{\sigma_{abs}}{A_{pump}}, \tag{S4}$$

where σ_{abs} and A_{pump} are the absorption cross-section of the nanosheet array and the spot size of the pump laser, respectively. σ_{abs} values were obtained through Finite Difference Time Domain (FDTD) simulation, where the nanosheet array was illuminated with a plane wave with 520 nm wavelength at normal incidence and the net power absorption in the nanosheets was measured. It is important to note that Equation S3 assumes a uniform distribution of carrier density across the entire active volume V. FDTD simulations, however, indicate that the pump laser absorption profile, which directly reflects the carrier generation profile, is not uniform across the entire nanosheet volume. As shown in Fig. S10a, both the TE and TM-polarised absorption profiles along the *yz*-plane of the nanosheets with α = 0.1 are highly concentrated near the top surface due to strong absorption in InP at this pump wavelength. As a result, the average integrated absorption along the *z*-axis of the nanosheets is highly non-uniform as well, as shown in Fig. S10b. To account for this non-uniformity in pump absorption, we define a parameter *m*, which is the height ratio at which 90 % of the total amount of absorbed pump power occurs. Table S1 lists the values of σ_{abs} and *m* for the devices with varying α values that are discussed in Fig. 4 of the main text. The active volume *V* is then estimated by multiplying the nanosheet volume by *m*.

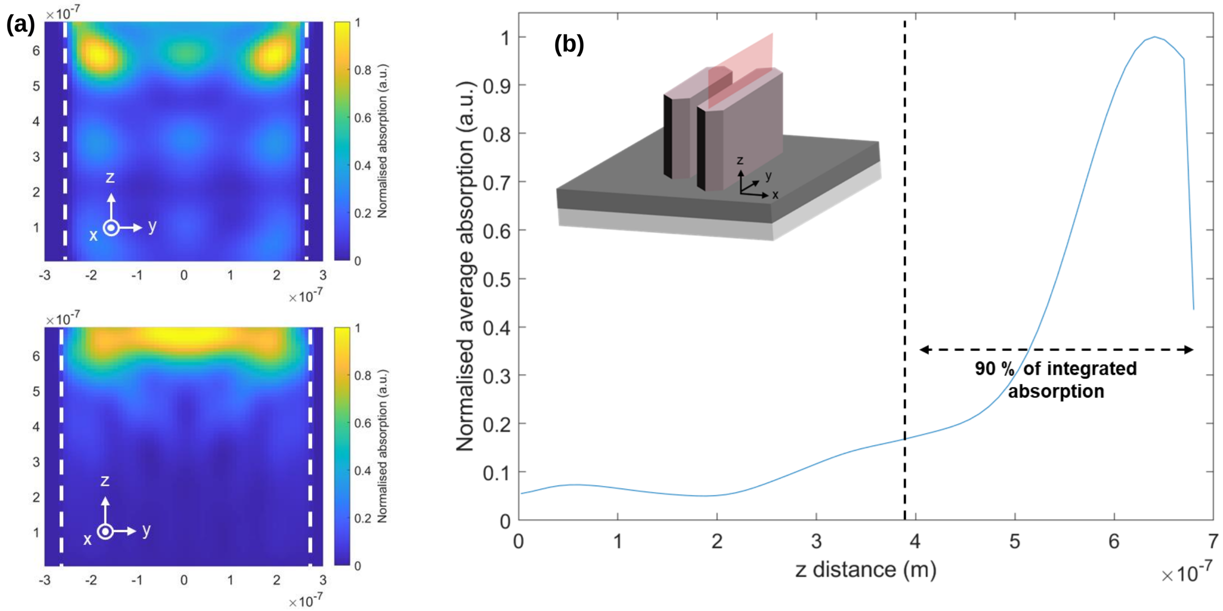

Fig. S10 Simulated pump absorption profiles in a nanosheet pair with α = 0.1. (a) *yz*-plane absorption profiles simulated across the centre plane of the nanosheet, as illustrated by the shaded plane in the schematic diagram in the inset of **(b)**. Top and bottom plots are the absorption profiles for TE and TM 520 nm plane wave illumination, respectively. **(b)** Average absorption profile along the *z*-axis of the nanosheet, obtained by averaging the absorptions with TE and TM illumination, then integrating over the nanosheet width in the *x* direction. The parameter *m* is defined as the ratio of the nanosheet height at which 90 % of the total integrated absorption occurs to the total nanosheet height. Inset is a schematic diagram that illustrates the *yz*-plane (shaded plane) where the nanosheet absorption was simulated.

With the values of E_g, *N*, and *T*, we can then calculate the quasi-Fermi levels in the conduction band and valence band by solving the charge-neutrality equation. The Fermi-Dirac distributions in Equation S1 can then be determined with the quasi-Fermi levels. Table S2 lists down all the material parameters used for gain modelling. Further gain modelling details can be found in our previous work[11].

Table S1 Simulated absorption cross-sections and *m* values for devices with varying values of α.

α	σ_{abs} (cm^2)	m
0.08	6.32×10^{-7}	0.53
0.10	6.28×10^{-7}	0.54
0.13	5.97×10^{-7}	0.55
0.15	5.92×10^{-7}	0.54
0.165	5.89×10^{-7}	0.57

Table S2 Material parameters used for WZ-phase InP gain modelling

Material parameter	Value
$\boldsymbol{n_r}$	3.4[6]
$\boldsymbol{E_p}$ $(\lvert \boldsymbol{M}\rvert^2 = \frac{\boldsymbol{m_0 E_p}}{\boldsymbol{6}})$	20.7 eV[6]
$\boldsymbol{E_B}$	1.545 eV[9]
$\boldsymbol{a}$	45 meV[9]
$\boldsymbol{\theta}$	238 K[9]
$\boldsymbol{m_e^*}$	$0.088m_0$[12,13]
$\boldsymbol{m_h^*}$	$0.37m_0$[12,13]

Section E: Solving laser rate equation

Experimental L-L curves were fitted by the following coupled rate equations, solved for the carrier density N and photon density S[14]:

$$\frac{dN}{dt} = \frac{\eta_{pump}\cdot P(t)}{E_{pump}V} - AN - BN^2 - CN^3 - v_g g(N)S \tag{S5a}$$

$$\frac{dS}{dt} = \Gamma\left[v_g\left(g(N) - g_{th}\right)S + \beta BN^2\right], \tag{S5b}$$

where the terms in Equation S5a, from left to right, represent the carrier generation rate, non-radiative carrier recombination rate, radiative carrier recombination rate, Auger recombination rate, and recombination rate due to stimulated emission. The terms in Equation S5b, from left to right, represent the net photon generation rate due to stimulated emission and the coupling between spontaneous emission and stimulated emission.

(a) Carrier generation rate

The 520 nm femtosecond pulsed laser used for optical pumping is modelled by the *P(t)* term in Equation S5a:

$$P(t) = P_{peak} sech^2\left(\frac{1.76t}{\Delta t}\right), \tag{S6}$$

where P_{peak} is the peak power of a single pulse and Δt is the pulse width of the laser, which is 200 fs. η_{pump}, E_{pump}, and *V* are defined similarly as in Equation S3.

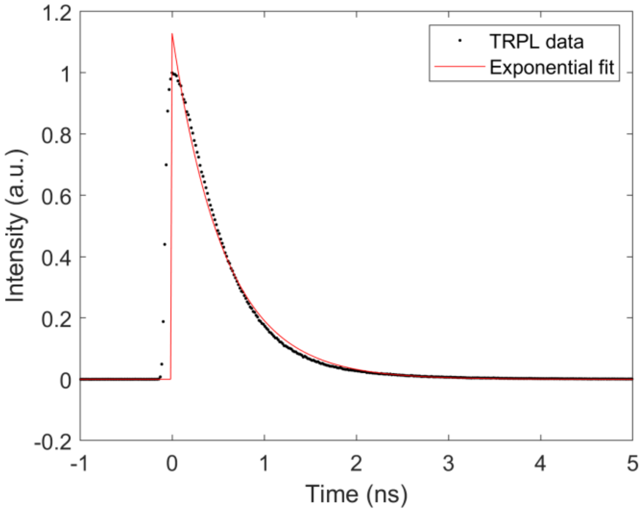

Fig. S11 PL decay signal measured at 870 nm with a pump fluence of around 0.1 μJ cm^{-2} pulse^{-1}. An exponential decay function with a decay constant of $\tau = 0.7$ ns is fitted to the experimental data.

(b) Recombination coefficients *A*, *B*, and *C*

The non-radiative recombination coefficient *A* is calculated from the non-radiative carrier lifetime τ_{nr} ($A = \tau_{nr}^{-1}$), which can be extracted from the PL decay signal measured at low excitation intensity where the carrier lifetime is dominated by non-radiative recombination. Fig. S11 shows the PL decay signal measured at a pump fluence of 0.1 μJ cm^{-2} pulse^{-1}. τ_{nr} of 0.7 ns is extracted by fitting an exponential decay function to the measured data. On the other hand, the radiative recombination coefficient *B* and Auger recombination coefficient *C* are adopted directly from the literature[15], which are 6.25×10^{-10} cm^3 s^{-1} and 9.1×10^{-31} cm^6 $^{s-1}$, respectively.

(c) Photon generation by stimulated emission

The stimulated emission terms in Equation S5 depend on the group velocity v_g, mode confinement factor Γ, and the material gain modelled as a function of the carrier density *g(N)*. v_g is given by c/n_g, where *c* and n_g are the speed of light in vacuum and the group refractive index of the lasing mode (estimated to be ~ 3.5 from FDTD simulations), respectively. Γ values were obtained from the FDTD-simulated electric field intensity profiles. The Γ values of devices with varying α values are listed in Table S3. $g(N)$ is modelled with a logarithmic function[14]:

$$g(N) = g_0 \ln\left(\frac{N+N_S}{N_{tr}+N_S}\right), \qquad \text{(S7)}$$

where g_0, N_s, and N_{tr} are fitting parameters obtained by fitting Equation S7 to gain curves calculated using Equation S1 at different levels of N at a given wavelength. We plot the $g(N)$ curves fitted at the lasing wavelengths for the devices with varying α values (discussed in Fig. 4 of the main text) in Fig. S12. The fitted values of g_0, N_{tr}, and N_s for these devices are listed in Table S4. As shown by Fig. S12 and Table S4, larger values of g_0 translates into larger slopes of the $g(N)$ curves, indicating faster increase in the material gain with the carrier density levels. Furthermore, the $g(N)$ curves in Fig. S12 also show that compared to the devices with smaller α values ($\alpha = 0.08$ and 0.10), the devices with larger α values ($\alpha = 0.13$, 0.15, and 0.165) have larger g_0 values, hence they are expected to attain their respective threshold gain levels g_{th} at smaller carrier density levels. This explains the lower lasing thresholds in these devices, as discussed in Fig. 4 of the main text. In Fig. S13, we plot the gain curves calculated at varying N levels together with the experimentally measured lasing peaks in devices with varying α values. From the plots, one can see that at the average g_{th} levels, the lasing peaks of the devices with larger a values have a better spectral overlap with the material gain peaks (indicated by the shaded region). This corresponds well to the larger slopes in the gain curves modelled as a function of the carrier density, as demonstrated in Fig. S12.

(d) Threshold gain level g_{th}

Along with the spontaneous emission factor β, g_{th} values are obtained by fitting the solutions of Equation S5 to experimental L-L data. g_{th} values reflect the quality of the lasing cavity and the gain material. Table S5 below summarises the fitted g_{th} values for all the devices discussed in Fig. 4 of the main text.

Table S3 Simulated mode confinement factors Γ for devices with varying values of α.

α	Γ
0.08	0.50
0.10	0.48
0.13	0.46
0.15	0.45
0.165	0.40

Table S4 ***g(N)*** **fitting parameters for devices with varying values of** α

α	Lasing wavelength (nm)	g_0 (cm^{-1})	N_{tr} (×10^{18} cm^{-3})	N_s (×10^{17} cm^{-3})
0.08	883	290.7	2.269	-2.123
0.10	880	387.2	2.284	-2.093
0.13	874	600.6	2.330	-1.990
0.15	870	871.0	2.415	-1.776
0.165	868	990.9	2.461	-1.646

Table S5 Fitted g_{th} **values for devices with varying values of** α**.**

α	g_{th} (cm^{-1})
0.08	75±5
0.10	75±5
0.13	78±5
0.15	80±5
0.165	95±5

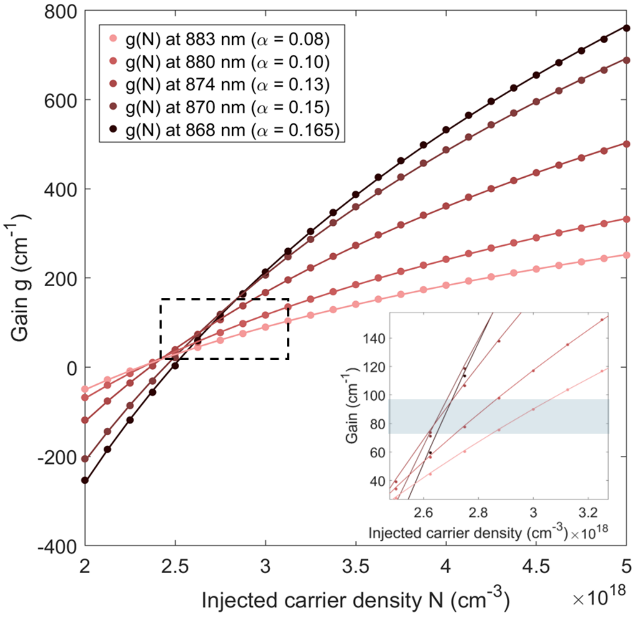

Fig. S12 Fitted ***g(N)*** **curves for devices with varying values of** α**.** g(N) curves were calculated with Equation S7 using the parameters listed in Table S4. Inset shows the magnified view near the threshold gain levels of the devices, which are indicated by the shaded region.

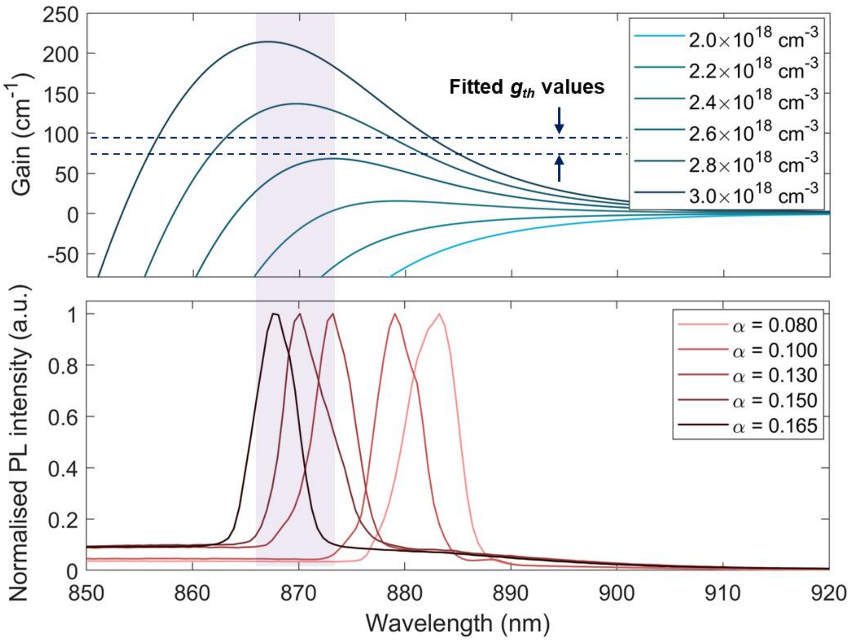

Fig. S13 Calculated material gain spectra of WZ-phase InP for varying levels of carrier density (top panel) and the lasing spectra measured in devices with varying α values at pump fluences approximately 20 % above the lasing thresholds of the respective devices (bottom panel). Dotted lines at the top panel indicate the range of g_{th} values obtained from fitting laser rate equation to the experimental L-L curves (see Table S5 for fitted g_{th} values). Shaded region is a guide to the eye that shows the optimal spectral overlap between the lasing peaks with larger α values and the gain curves at gain values near the fitted g_{th} of the devices.

Section F: Additional optical measurement and simulation data

In this section, we provide additional optical measurement and simulation data, including the pre-lasing PL data for the α = 0.10 device, carrier lifetime measurements, lasing mode profile simulation, and lasing measurements performed on the device with α = 0. Fig. S14a shows the room-temperature PL spectrum measured in the α = 0.10 device at a relatively low pump fluence below its lasing threshold. The device exhibits a broad emission spectrum peaking at around 870 nm, which fits well with the calculated fundamental band-to-band spontaneous emission in bulk wurtzite (WZ)-phase InP (see Methods of the main text for spontaneous emission modelling details). The spontaneous emission spectrum then gradually broadens with increasing pump fluences, indicating band-filling at higher injected carrier densities, as shown in Fig. S14b. At a pump fluence of around 18 μJ cm^{-2} pulse^{-1}, a narrow peak emerges at around 880 nm, with the SE intensity saturating with further increase in the pump fluence, implying threshold gain clamping and a transition from spontaneous emission into the amplified spontaneous emission (ASE) regime.

Further evidence of lasing was also acquired by studying the carrier dynamics of the device at varying excitation intensities. As shown by the temporal PL decay signals in Fig. S15, with increasing pump fluences below the lasing threshold, the carrier lifetime τ shortens modestly from

0.565 to 0.318 ns due to increasing spontaneous emission rate at higher carrier densities. These lifetime values are comparable to the non-radiative lifetime of around 0.7 ns (see Fig. S11 for τ_{nr} measurement). Since τ is given by:

$$\tau^{-1} = \tau_r{}^{-1} + \tau_{nr}{}^{-1}, \tag{S8}$$

where τ_r and τ_{nr} are the radiative and non-radiative lifetimes, respectively, this implies comparable contributions from both the non-radiative and radiative recombination processes in carrier depletion in this regime. A stark change in the carrier dynamics occurs at pump fluences beyond lasing threshold, where τ is reduced by at least an order of magnitude to below the system limit of around 29 ps, indicating that τ_r now dominates Equation (S8). More importantly, the dramatic reduction in τ_r at pump fluences below and above lasing threshold reflects a transition in the emission mechanism from spontaneous emission to the much faster stimulated emission, further corroborating lasing action in the device[4,16].

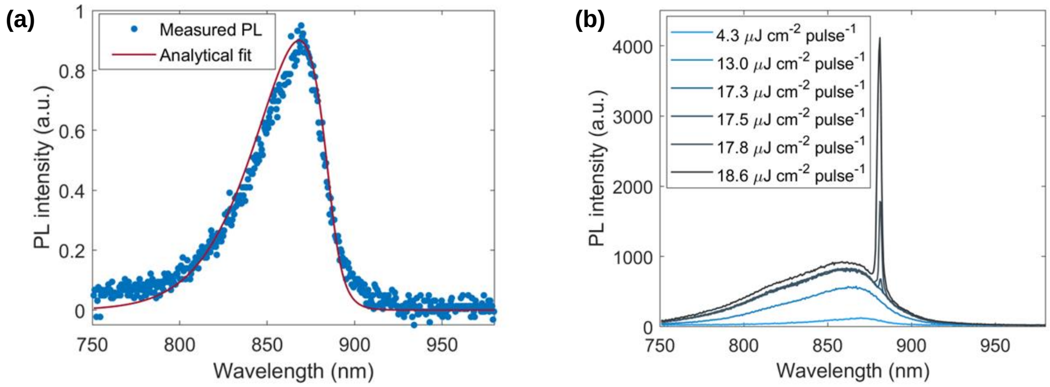

Fig. S14 Room-temperature PL measurements before and just at the onset of lasing. (a) PL spectrum measured at a low pump fluence (~ 30 % of the lasing threshold), fitted with an analytical expression for spontaneous emission from WZ-phase InP at room-temperature. **(b)** Power-dependent PL spectra measured at pump fluences ranging from below to just above lasing threshold, showing spontaneous emission clamping and emission linewidth narrowing near 18 μJ cm^{-2} pulse^{-1}.

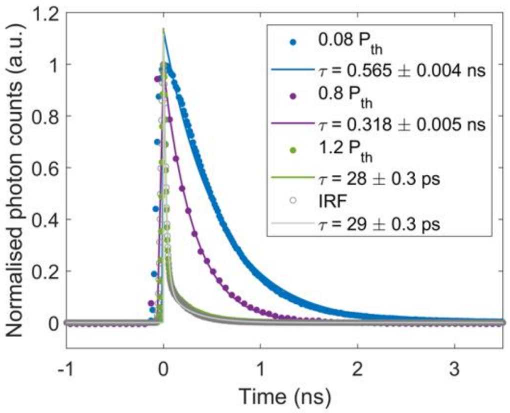

Fig. S15 PL decay signals measured at the lasing wavelength at various pump fluence levels. The signals are fitted with exponential decay functions to extract the carrier lifetime. The instrument response function (IRF) of the system is also shown as a reference.

To identify the lasing mode, we numerically simulated the field distribution profiles of the lasing mode at 880 nm in Fig. S16. To realistically model the optically pumped device, we considered a finite photonic crystal with 16×16 unit cell periods, surrounded by a boundary of unpumped (lossy) unit cells (see Methods of the main text for further details). The simulation results indicate that the fields of the lasing mode concentrate around the centre of the pumped region, with vanishing field enhancement near the pump boundaries. This can be explained by the enhanced in-plane leakage losses caused by the finite excitation area. Despite the additional in-plane losses, 16×16 periods of unit cells are still sufficient to support the intended 2D standing wave in the pumped region, as evidenced by the simulated electric field intensity profile in Fig. S16 (a). The *z*-oriented magnetic field vector profile, shown in Fig. S16 (b), also confirms the identity of the lasing mode to be the designed quasi-BIC mode. Importantly, the simulated near-field enhancement profile of the lasing mode is in good qualitative agreement with the spatially-resolved emission profiles measured in the device, as discussed in Fig. 3 of the main text.

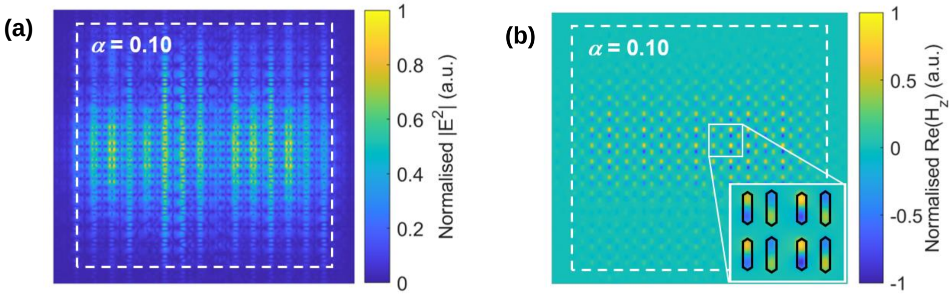

Fig. S16 Simulated field distribution profiles of the device with $\alpha = 0.10$ at the lasing wavelength of 880 nm. The simulated device has a finite array with 16×16 periods of active unit cells (assumed to be pumped to transparency), surrounded by a boundary of unpumped (lossy) nanosheet pairs, as indicated by the white dotted lines. **(a)** and **(b)** are the normalised electric field intensity profile and the *z* vector component of the magnetic field, respectively. Inset in **(b)** shows a magnified view of the field distribution in four nanosheet pairs.

Next, we briefly discuss the lasing measurement results performed on the device with $\alpha = 0$ (SEM images of the fabricated devices shown in Fig. S17). Fig. S18a shows the power-dependent PL spectra and the normalised PL spectral map measured in the device at room-temperature. A lasing peak at around 897 nm was detected in the device with a lasing threshold of around 20 μJ cm^{-2} pulse^{-1}, closely matching the simulated BIC resonant wavelength with $\alpha = 0$. In addition, Fig. S18b shows the back focal plane image measured in the device at a pump fluence of around 20 % above its lasing threshold. Compared to the other devices with non-zero α values that are discussed in the main text (see Fig. S9), this device shows a much weaker emission at normal incidence (relative to the spontaneous emission background and the ASE emission most likely from the TE side mode), indicating that the BIC lasing mode couples very weakly to far-field radiation. This also implies that BIC mode lasing most likely occurs due to slight fabrication imperfection in the device.

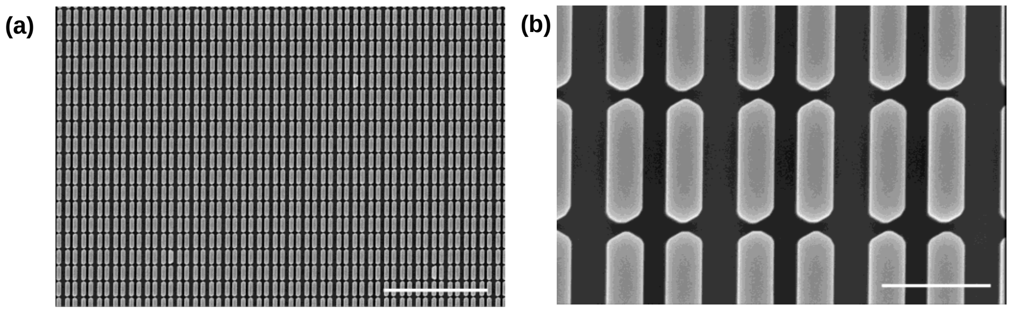

Fig. S17 Top-view SEM images of the device with $\alpha = 0$. Scale bars in **(a)** and **(b)** are 4 μm and 500 nm, respectively.

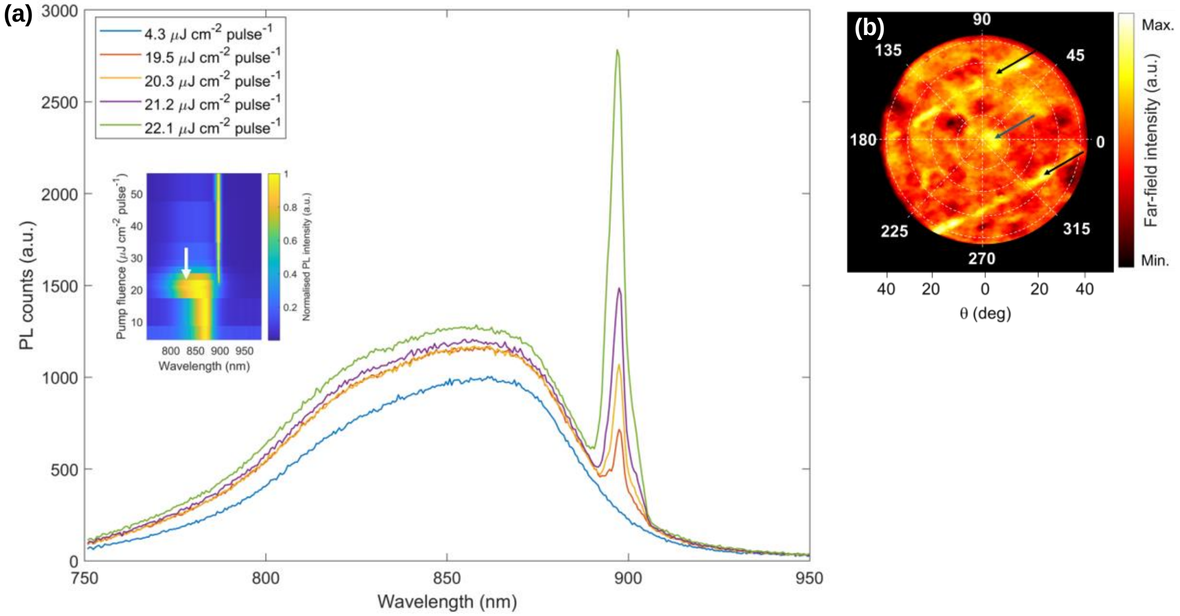

Fig. S18 Lasing characteristics of the $\alpha = 0$ device. (a) Power-dependent PL spectra measured in the device at room-temperature. Inset shows the normalised PL spectral map, with the white arrow indicating the amplified spontaneous emission shoulder due to coupling to the TE side mode. (b) Back focal plane image measured at a pump fluence around 20 % above the lasing threshold. The emission hotspot near $\theta = 0°$ (indicated by the blue arrow) corresponds to lasing emission via the quasi-BIC mode. The black arrows indicate two side lobes around the centre beam, most likely corresponding to the ASE-coupled TE side mode.

References

1. Wang, N. *et al.* Understanding shape evolution and phase transition in InP nanostructures grown by selective area epitaxy. *Small* **17**, 2100263 (2021).
2. Gautam, C. *et al.* Mode distribution impact on photonic crystal surface emitting laser performance. *APL Photonics* **9**, 076113 (2024).
3. Messina, C. *et al.* Deformed Honeycomb Lattices of InGaAs Nanowires Grown on Silicon-on-Insulator for Photonic Crystal Surface-Emitting Lasers. *Adv. Opt. Mater.* **11**, 2201809 (2023).
4. Ren, Y. *et al.* Low-threshold nanolasers based on miniaturized bound states in the continuum. *Sci. Adv.* **8**, eade8817 (2022).
5. Tang, R. *et al.* Two-dimensional heterostructure quasi-BIC photonic crystal surface-emitting laser with low divergence. *Nanophotonics* **12**, 3257–3265 (2023).
6. Chuang, S. L., Peyghambarian, N. & Koch, S. *Physics of Optoelectronic Devices*. *Wiley Series in Pure and Applied Optics* (John Wiley & Sons, 1995). doi:10.1063/1.2807693
7. Saxena, D. *et al.* Optically pumped room-temperature GaAs nanowire lasers. *Nat. Photonics* **7**, 963–968 (2013).
8. De Luca, M. *et al.* Polarized light absorption in wurtzite InP nanowire ensembles. *Nano Lett.* **15**, 998–1005 (2015).
9. Zilli, A. *et al.* Temperature dependence of interband transitions in wurtzite InP nanowires. *ACS Nano* **9**, 4277–4287 (2015).
10. Gadret, E. G. *et al.* Valence-band splitting energies in wurtzite InP nanowires: Photoluminescence spectroscopy and ab initio calculations. *Phys. Rev. B - Condens. Matter Mater. Phys.* **82**, 125327 (2010).
11. Wong, W. W., Su, Z., Wang, N., Jagadish, C. & Tan, H. H. Epitaxially grown InP micro-ring lasers. *Nano Lett.* **21**, 5681–5688 (2021).
12. Tedeschi, D. *et al.* Value and Anisotropy of the Electron and Hole Mass in Pure Wurtzite InP Nanowires. *Nano Lett.* **16**, 6213–6221 (2016).
13. Tedeschi, D. *et al.* Hole and Electron Effective Masses in Single InP Nanowires with a Wurtzite-Zincblende Homojunction. *ACS Nano* **14**, 11613–11622 (2020).
14. Coldren, L. A. & Corzine, S. W. *Diode Lasers and Photonic Integrated Circuits*. *Wiley-Interscience* (John Wiley & Sons, 1997). doi:10.1117/1.601191
15. Markvart, T. & Castaner, L. *Practical Handbook of Photovoltaics: Fundamentals and Applications*. (Elsevier, 2003).
16. Wu, M. *et al.* Room-Temperature Lasing in Colloidal Nanoplatelets via Mie-Resonant Bound States in the Continuum. *Nano Lett.* **20**, 6005–6011 (2020).